Efficient Hybrid Mixed Ion Perovskite Photovoltaics: *In Situ* Diagnostics of the Roles of Cesium and Potassium Alkali Cation Addition

Ming-Chun Tang[1,5,7‡*], Yuanyuan Fan[2‡], Dounya Barrit[1], Ruipeng Li[4], Hoang X. Dang[3], Siyuan Zhang[5,8], Timothy Magnanelli[5], Nhan V. Nguyen[5], Edwin J. Heilweil[5], Christina A. Hacker[5], Detlef-M. Smilgies[6], Kui Zhao[2*], Aram Amassian[1,3*] and Thomas D. Anthopoulos[1*]

[1]King Abdullah University of Science and Technology (KAUST), KAUST Solar Center (KSC), and Physical Science and Engineering Division (PSE), Thuwal, 23955-6900, Saudi Arabia

[2]Key Laboratory of Applied Surface and Colloid Chemistry, National Ministry of Education, Shaanxi Key Laboratory for Advanced Energy Devices, and Shaanxi Engineering Lab for Advanced Energy Technology, School of Materials Science and Engineering, Shaanxi Normal University, Xi'an 710119, China

[3]Department of Materials Science and Engineering, North Carolina State University, Raleigh, NC, 27695, USA

[4]Brookhaven National Laboratory (BNL), Upton, NY 11973, USA

[5]Physical Measurement Laboratory, National Institute of Standards and Technology (NIST), Gaithersburg, MD 20899, USA

[6]Cornell High Energy Synchrotron Source (CHESS), Cornell University, Ithaca, NY 14850, USA

[7]Institute for Research in Electronics and Applied Physics & Maryland NanoCenter, University of Maryland, College Park, MD 20742, USA

[8]Theiss Research, La Jolla, CA 92037, USA

‡ M.-C. Tang and Y. Fan contributed equally to this work.

Keywords: *In situ* GIWAXS; mixed cations and halides perovskite solar cells; incorporation of cesium and potassium cations; ambient stability.

Abstract

Perovskite photovoltaics have made extraordinary progress in power conversion efficiency (PCE) and stability owing to process and formulation development. Perovskite cell performance benefits from the addition of alkali metal cations, such as cesium (Cs^+) and potassium (K^+) in mixed ion systems, but the underlying reasons are not fully understood. Here, we study the solidification of perovskite layers incorporating 5, 10, to 20% of Cs^+ and K^+ using *in situ* grazing incidence wide-angle X-ray scattering. We found that K^+-doped solutions yield non-perovskite 4H phase rather than the 3C perovskite phase. For Cs^+-doped formulations, both 4H and 3C phases are present at 5% Cs^+, while the 3C perovskite phase forms in 10% Cs^+-doped formulations, with undesirable halide segregation occurring at 20% Cs^+. Post-deposition thermal annealing converts the intermediate 4H phase to the desirable 3C perovskite phase. Importantly, perovskite layers containing 5% of Cs^+ or K^+ exhibit reduced concentration of trap states, enhanced carrier mobility and lifetime. By carefully adjusting the Cs^+ or K^+ concentration to 5%, we demonstrate perovskite cells with a ≈5% higher average PCE than cells utilizing a higher cation concentrations. The study provides unique insights into the crystallization pathways towards perovskite phase engineering and improved cell performance.

Introduction

Hybrid organic-inorganic metal-halide perovskites prepared via low-cost solution-processing approaches have demonstrated remarkable optoelectronic properties, including a low exciton binding energy, a small Urbach energy, and sharp absorption onset.[1] Hybrid perovskites feature the characteristic AMX_3 structure, where A^+ is a monovalent organic or inorganic cation, most often methylammonium (MA^+), formamidinium (FA^+), cesium (Cs^+), potassium (K^+), rubidium (Rb^+), or their mixtures. M^{2+} metal cations are limited to lead (Pb^{2+}) and/or tin (Sn^{2+}), and X^- is a monovalent halide anion such as chloride (Cl^-), bromide (Br^-), iodide (I^-), or their mixtures.[2] Perovskite thin films are most commonly processed through a one-step spin-coating method, whereby an antisolvent is dripped at an optimal time during spin coating, and the resulting film is subsequently annealed to convert to the desirable perovskite phase. Planar heterojunction perovskite photovoltaics prepared using the one-step spin-coating process and combining careful interfacial engineering and contact passivation have recently surpassed the power conversion efficiency (PCE) milestone of 25%.[3]

Substantial effort has been put into improving device PCE and stability[4], which have mainly been driven by the perovskite thin film morphology and microstructure, which in turn influence optoelectronic properties including carrier mobility and trap state density.[5] The research focus of 3D hybrid perovskites has therefore evolved from the classic $MAPbI_3$ to mixed cation (containing Cs^+, Rb^+ and/or K^+) and mixed halide (I^- and Br^-) perovskites which appear to improve solar cell performance and long-term stability.[6] For instance, Segawa's group reported that a small amount of K^+ incorporated into the perovskite absorber was able to significantly improve the PCE of solar cells and diminish current-voltage hysteresis.[7] Saliba *et al.* presented, with the addition of Cs^+, the resulting triple-cation (Cs^+/ FA^+/ MA^+) perovskites are thermally more stable and contain fewer phase impurities, which enable a stabilized PCE output of 21.1%.[8] However, despite the simplicity of implementation of the one-step deposition process, the mechanisms underlying microstructure development and phase transformation pathway, from precursor inks to solid-state films, are remarkably complex and still poorly understood. This is partially due to insufficient information on phase transformation behavior and the formation of intermediate phases observed through *ex situ* characterization approaches. Thus, the capability to investigate the solution processing of perovskite thin film deposition via *in situ* techniques becomes an

essential capability to shed light on the crystallization pathway and its relation to microstructure, morphology, optoelectronic properties, and ultimately enable translation to scalable manufacturing processes.

Recently, *in situ* grazing incidence wide-angle X-ray scattering (GIWAXS) has emerged as a practical approach to study solid-state thin film formation and microstructure evolution during solution casting of solution-based semiconductors.[9] *In situ* GIWAXS performed during solution-based coating has also been utilized successfully to investigate crystallization behavior for 3D and reduced dimensional perovskites via spin-coating and blade-coating.[9a-f, 10] Gong *et al.* examined classic $MAPbI_3$ ink during mini-slot-die printing by using *in situ* GIWAXS, which indicated the formation of disordered solvated nanoparticles (sol), as well as solvated crystalline intermediates, and the polycrystalline perovskite phase.[11] In the two-step perovskite deposition method, time-resolved GIWAXS results reveal a sol–gel process involving three PbI_2-solvent complexes formation and appropriate solvated state of PbI_2 exposed to MAI can lead to rapid and complete room temperature conversion into higher quality $MAPbI_3$ films with improved solar cell performance.[12] Most recently, FA^+-dominated mixed cations and mixed halides perovskites ($FA_{1-x-y}MA_xCs_yPbI_{3-z}Br_z$ and $FA_{1-x-y}MA_xK_yPbI_{3-z}Br_z$) have recently demonstrated superior device performance and stability compared to the classic $MAPbI_3$ and $FAPbI_3$ cases. The roles of Rb^+ and Cs^+ addition alone or together have been shown to alter the phase transformation pathway and promote the direct formation of the hybrid perovskite phase.[6a, 9e, 13] However, the impacts of Cs^+ and K^+ additions in perovskite inks on the phase transformation pathway, microstructure and optoelectronic properties for fabricating high-efficiency perovskite solar cells have not been understood comprehensively. Understanding phase transformation of MA^+- and FA^+-dominated perovskites and their differences in the presence of small amounts of Cs^+ or K^+ addition is essential for future perovskite ink designs and to enable hybrid perovskite printed optoelectronic device manufacturing.

Here, we study representative $FA_{0.85-x}MA_{015}K_xPbI_{2.55}Br_{0.45}$ and $FA_{0.85-y}MA_{015}Cs_yPbI_{2.55}Br_{0.45}$ (x and y = 0.05, 0.1, and 0.2, respectively) perovskite inks and explore the phase transformation via *in situ* GIWAXS measurements. The approach allows unveiling the relationship between the solidification pathway and alkali metal cations doping. We adopt widely employed nomenclature proposed by Gratia *et al.* for metal oxide perovskite polytypes.[14] K^+-

doped films naturally form intermediate non-perovskite 4H phases without the desired 3C perovskite phase. The 3D polytype non-perovskite 4H phase may structurally be derived from the pure hexagonal close-packed 1D delta phase (infinite face-sharing PbI_6 octahedra) and metallate-solvent complexes but is more complicated due to higher dimensionality. Heavier I^- anion preferentially occupies the face-sharing position in hexagonal 4H perovskite polytype and the crystallization pathway may be triggered by bromide to iodide exchange in the 2H phase, breaking up the face sharing connectivity of the 2H phase.[14] In contrast, 5% Cs^+ films form 4H and polycrystalline 3C perovskite phases simultaneously. In the 10% Cs^+-doped solution, the 3C perovskite phase is the dominant microstructure during spin coating. However, perovskite halide segregation occurs in high 20% Cs^+ concentration and results in poor device performance. Thermal annealing treatment converts 4H into the desired 3C phase. Low concentration Cs^+ or K^+ in perovskites remediates trap states, enhances carrier mobility, and increases carrier lifetime. Using these insights, we achieved maximum/average PCEs of 20.8%/19.5% for $FA_{0.75}MA_{0.15}Cs_{0.1}PbI_{2.55}Br_{0.45}$ devices.

Results and discussion

To understand the impact of Cs^+ and K^+ alkali metal cation concentration on the phase transformation behavior during spin coating, we perform time-resolved grazing-incidence wide-angle X-ray scattering (GIWAXS) measurements on $FA_{0.85-x}MA_{0.15}K_xPbI_{2.55}Br_{0.45}$ and $FA_{0.85-y}MA_{0.15}Cs_yPbI_{2.55}Br_{0.45}$ (x and y = 0.05, 0.1, and 0.2 respectively) perovskite solutions in the solvent mixture of N,N-dimethylformamide (DMF) and dimethyl sulfoxide (DMSO) (4:1 volume ratio). These *in situ* GIWAXS measurements excluded antisolvent drip as they aim at a more profound understanding of different concentrations of K^+ and Cs^+ on the unquenched phase transformation behavior in order to comprehend the roles of these alkali metal cations better. **Fig. 1a and b** show the scattering intensity (integrated over each time slice, 0.2 s) with respect to q (ordinate; $4 < q < 12$ nm^{-1}) and spin-coating time (abscissa; $0 < t < 240$ s). The length of the scattering vector q is determined by the following equation: $q = \sqrt{q_z^2 + q_{xy}^2}$, where $q_z = \frac{4\pi sin\alpha_f}{\lambda}$, $q_{xy} = \frac{4\pi sin\theta_f}{\lambda}$, and λ is the wavelength.[9d] The emergent waves with the momentum can be described by in-plane exit angle α_f and out-of-plane angle θ_f (with respect to scattering plane).[15]

Representative 2D GIWAXS snapshots collected at 40 s, 160 s, and 240 s during spin coating without an antisolvent drip of all perovskite formulations are also shown in **Fig. S1 and S2**.

Fig. 1a demonstrates representative time-evolution of the scattering features with respect to q during spin coating for $FA_{0.85-x}MA_{0.15}K_xPbI_{2.55}Br_{0.45}$ (x = 0.05, 0.1, and 0.2) nominal formulation. The intermediate non-perovskite phases such as hexagonal well-established Ramsdell notation 2H, 4H, and 6H are often referred to as δ phase, while the cubic 3C perovskite phase is referred to as α phase.[16] In the case of 5% K^+ doped (x = 0.05) formulations, we observe the scattering halo at low q values ($q \approx 4$ to 7 nm^{-1}),[6a] which is attributed to the sol consisting of metallate-solvent complexes, such as between iodoplumbates and bromoplumbates and DMSO as well as DMF solvent molecules.[17] The scattering from the sol can be seen to extend to ≈180 s, then decays rapidly, while the formation of the non-perovskite 4H (100) phase (q = 8.4 nm^{-1}) appears at ≈160 s. The (101) reflection of the 4H phase (q = 9.2 nm^{-1}) appears at a later time ≈200 s, which suggests this polytype may be textured and a different orientation begins to form upon further removal of solvent from the sol. The scattering intensity of the 4H reflections is weak, indicating that the as-cast film is highly disordered. Furthermore, increasing [K^+] resulted in a considerably longer-lived sol state, which appears to be stabilized with the addition of this alkali halide. This is indicated by the sustained sol scattering and the delayed onset of formation of 4H (100) and (101) reflections, which is delayed to ≈200 s. To sum up, as-cast formulations of $FA_{0.85-x}MA_{0.15}K_xPbI_{2.55}Br_{0.45}$ (x = 0.05, 0.1, and 0.2) yield the non-perovskite 4H phase exclusively, without observation of the desired 3C (100) perovskite phase. The sol state appears to be stabilized by the presence of K^+.

Substituting K^+ with Cs^+ in $FA_{0.85-y}MA_{0.15}Cs_yPbI_{2.55}Br_{0.45}$ (y = 0.05, 0.1, and 0.2) formulations results in vastly different solidification and crystallization pathways (**Fig. 1b**). The disordered colloidal sol scattering is qualitatively similar to K^+ counterparts, albeit exhibiting stronger scattering at 5% Cs^+, and reduced scattering intensity with increasing [Cs^+]. This indicates that strong interactions exist between metallates and the solvent, as in the K^+ case.[18] However, unlike the K^+ case, Cs^+ addition forms the desired 3C perovskite phase [(100) reflection at q = 10.1 nm^{-1}] concurrently with weak the non-perovskite 4H phase [(100) and (101) reflections] at the ≈160 s mark. Importantly, increasing Cs^+ content from 5% to 10% appears to weakens the 4H (100) and the 3C (100) reflections and suppresses the 4H (101) reflection. Upon further doubling the Cs^+

content to 20%, the as-cast film appears to suppress the formation of the 4H phase to the benefit of the 3D phase. However, GIWAXS measurements reveal the formation of a doublet peak for 3C, which is consistent with the formation of a more I-rich phase (α_1 phase at q = 9.8 nm^{-1}) than the nominal formulation and a more Br-rich phase (α_2 phase at q = 10.3 nm^{-1}) than the nominal formulation (**Fig. 1c**). The formation of such a doublet is consistent with prior studies of mixed halide systems and indicative of crystallization-induced halide segregation.[6a, 9e, 13] Bromoplumbates tend to complex more weakly with polar solvents such as DMF and DMSO and form metal-rich clusters, whereas iodoplumbates complex strongly with DMSO.[17] To explain perovskite halide segregation, it is reasonable to assume that a slow-drying sol containing a mixture of iodoplumbates and bromoplumbates complexed with DMSO and DMF promotes halide segregation by preferential loss of solvent from Br^--rich regions while I^--rich areas remain highly solvated, thus promoting the formation of Br^--rich and relatively Br^--poor regions and leading to the formation of phases with different halide composition, as previously shown.[17-18]

To compare the overall differences in phase formation and microstructure in the as-cast films containing K^+ and Cs^+ after 240 s of spin-coating, **Fig. 1c** illustrates the diffraction intensity plots versus q at the end of the coating process, indicating the position and intensity of each associated phase. In addition, photographs of as-cast thin films based on these solutions are included as well (**Fig. 1d**). Comparing the formulations with 5% K^+ or Cs^+, it seems that 5% Cs^+ addition modifies the non-perovskite 4H texture by reducing (100) reflection and intensifying the (101) reflection. Concurrently, this promotes 3C phase formation, which does not occur with any amount of K^+ addition studied herein. It is not surprising to find that as-cast films with 5% K^+ appear light orange, whereas 5% Cs^+ renders a grayish due to perovskite phase formation. Increasing the alkali halide content to 10%, we find that K^+ forms a different texture of 4H and more overall scattering intensity, which is ascribed to the darker orange color of the sample. In contrast, 10% Cs^+ weakens 4H (100) but 3C (100) reflection is present, resulting in a darker brown color. Increasing alkali halides to 20%, we observe K^+ promotes the formation of 4H with (100) and (101) reflections now more prominent and the sample taking on a deep orange color. In contrast, 20% Cs^+ turns the as-cast film to a black color, which is a telltale sign of significant 3C perovskite phase formation even without annealing and antisolvent drip. To sum up, all $FA_{0.85-x}MA_{0.15}K_xPbI_{2.55}Br_{0.45}$ formulations studied yielded the non-perovskite 4H phase with sample color ranging from light orange to deep orange with increased [K^+]. In contrast, $FA_{0.85-}$

$_{y}MA_{0.15}Cs_{y}PbI_{2.55}Br_{0.45}$ formulations promoted the formation of the 3C perovskite phase with increasing [Cs^+] up to 20% in as-cast films, albeit resulting in halide segregation due to simultaneous formation of iodide- and bromide-rich perovskite phases.

Antisolvent treatment is a staple of the one-step spin-coating process and has been shown to play an essential role in mediating the phase transformation of perovskite films, including to yield higher quality films with better photovoltaic performance.[6a, 9f, 13] We have previously shown the antisolvent drip to promote immediate phase transformation and often results in a different phase transformation outcome than as-cast films which have not been subjected to it.[6a] Thus, it is critical to investigate the role of antisolvent drip as well and the interplay of drip and alkali halide additives, such as K^+ and Cs^+. To do so, we have performed the exact same investigations for $FA_{0.85-x}MA_{0.15}K_xPbI_{2.55}Br_{0.45}$ and $FA_{0.85-y}MA_{0.15}Cs_yPbI_{2.55}Br_{0.45}$ (x and y = 0.05, 0.1, and 0.2) formulations during spin-coated with the addition of a chlorobenzene (CB) antisolvent drip at ≈20 s (**Fig. 2a and b**). Representative 2D GIWAXS snapshots collected at 10, 120, and 240 s during spin coating with CB drip ≈20 s of all perovskite formulations are once again summarized in supporting information (**Fig. S3 and S4)**. **Fig. 2a** shows the time-evolution of phase transformation for 5, 10, and 20% K^+ cases with a CB drip at 20 s. We observe the low *q* scattering characteristic of disordered precursor sol, which does not appear to be significantly disrupted by the antisolvent drip, unlike K^+-free systems previously investigated.[6a] Following CB drip, however, the 4H phase appears after different delays following the drip and is delayed with increasing [K^+]. In all cases, the phases formed are associated with 4H, and the desirable 3C perovskite phase is not observed. The role of K^+ appears to be that of stabilizing the as-cast sol from being impacted by the antisolvent drip.

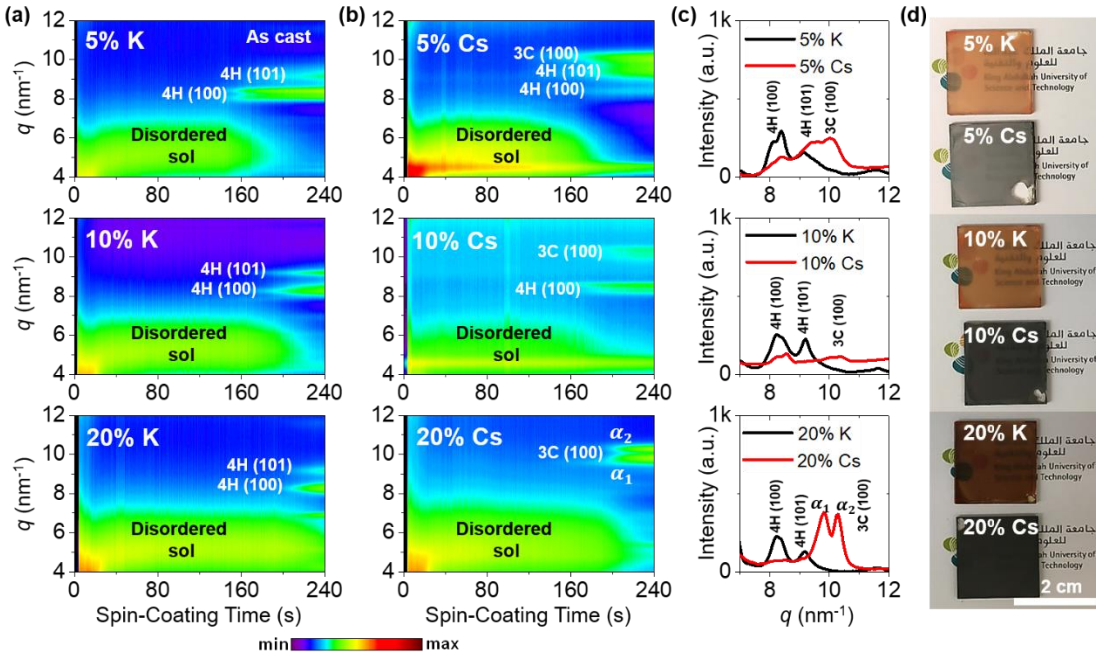

Figure 1. *In situ* time-resolved x-ray scattering intensity map of the various precursor formulations showing ink-to-solid film transformation behavior during spin coating for (a) $FA_{0.85-x}MA_{0.15}K_xPbI_{2.55}Br_{0.45}$ and (b) $FA_{0.85-y}MA_{0.15}Cs_yPbI_{2.55}Br_{0.45}$ (x and y = 0.05, 0.1, and 0.2 respectively). Together with (c) intensity distribution vs. scattering vector q for the same films at the final stage of spin coating (t = 240 s). Scattering features associated with the disordered colloidal sol, the non-perovskite 4H phase [(100): q = 8.4 nm^{-1}, (101): q = 9.2 nm^{-1}] are identified along with (100) reflection of the 3C perovskite phase (q = 10.1 nm^{-1}). For 20% Cs^+, an I-rich (α_1 phase, q = 9.8 nm^{-1}) and Br-rich (α_2 phase, q = 10.3 nm^{-1}) 3C phases are identified, indicating crystallization-induced halide segregation. (d) Photographs of the same as-cast thin films.

On the other hand, substituting K^+ with Cs^+ (**Fig. 2b**) has the opposite effect as the CB drip promotes the formation of solid phases immediately. The non-perovskite 4H (100) reflection is observed first, but this quickly gives way to the formation of the 3C perovskite phase together with 4H (101) reflection for 5% Cs^+ ink. The drip sees the 4H phase initially formed become consumed by or convert into the perovskite phase. Importantly, the 3C perovskite phase's (100) reflection, which was not prominent without drip, is very prominent with drip and consists of a single type of halide composition. Increasing [Cs^+] to 10%, the 3C perovskite appears to form directly from the

disordered sol precursor without showing evidence of any other phases on the time resolution of these measurements and no evidence of multiple 3C perovskite phases. However, it appears that 20% Cs^+ in the formulation is excessive and deleterious as this promotes the formation of two (100) reflections for the 3C phase, associated to an I-rich (α_1, q = 9.8 nm^{-1}) and a Br-rich (α_2, q = 10.3 nm^{-1}) perovskite phases.

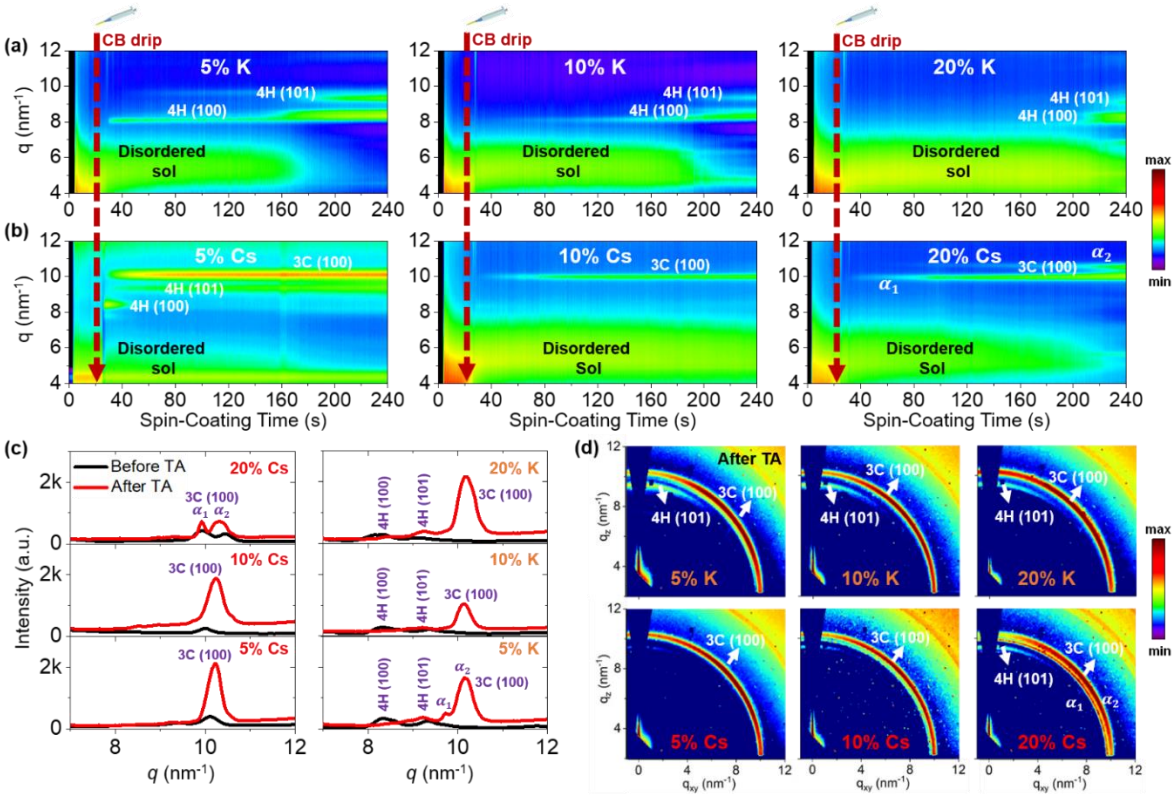

Figure 2. Time-resolved GIWAXS intensity maps of the various perovskite precursor inks showing ink-to-solid transformation during spin coating with antisolvent drip occurring at 20 s for (a) $FA_{0.85-x}MA_{0.15}K_xPbI_{2.55}Br_{0.45}$ and (b) $FA_{0.85-y}MA_{0.15}Cs_yPbI_{2.55}Br_{0.45}$ (x and y = 0.05, 0.1, and 0.2 respectively, from left to right). (c) Representative 2D GIWAXS images were taken after TA for each thin film. (d) Intensity distribution plot versus the scattering vector q for K^+- and Cs^+-containing (5, 10, and 20 %) perovskite thin films before and after TA. Scattering features associated with the disordered precursor sol, the yellow non-perovskite 4H phase [(100): q = 8.4 nm^{-1} and (101): q = 9.2 nm^{-1}] are identified along with 3C perovskite phase [(100): q = 10.1 nm^{-1}]. I-rich (α_1 phase, q = 9.8 nm^{-1}) and Br-rich (α_2 phase, q = 10.3 nm^{-1}) 3C perovskite phase (100) reflections are also identified.

These results prove that halide segregation can be mitigated by the drip for low and intermediate Cs^+ contents, but occurs for high concentration (20%) of Cs^+, whether a drip is used or not. This halide segregation leads to the coexistence of perovskite 3C phases exhibiting different bandgap and energetics, which thus creates recombination sites with a negative consequence on the performance of solar cells. Therefore, the choice of alkali metal cations, their concentration, and the role of antisolvent drip have a tremendous impact on the phase transformation process and microstructural outcome of the solution-coating process. This provides rational insights into the design of perovskite formulations for usage in optoelectronic applications.

Fig. 2c shows representative 2D GIWAXS snapshots collected after thermal annealing (TA, 100 ℃ for 10 min) together with the intensity distribution plots vs. scattering vector *q* for these perovskite films before and after TA (**Fig. 2d**). As expected, TA promotes the conversion of non-perovskite phases into the 3C perovskite phase. However, TA does not reverse the halide segregation observed in as-cast films with 20% Cs^+. For all different K^+-incorporated films (5, 10, and 20%), the 3C phase forms but does not completely convert the 4H phase after TA, which is likely to harm solar cell performance by reducing the volume of photoactive materials and acting as recombination sites.

We summarize the microstructural findings for as-cast and thermally annealed samples subjected to antisolvent drip in **Table 1**. K^+-doped films, prior to TA, tend to form the 4H phase from the disordered solvate without the desired 3C perovskite crystal formation. TA converts the 4H phase into the desirable 3C perovskite phase, highlighting the necessity of TA for completing the perovskite phase conversion, as evidenced by *ex situ* GIWAXS and XRD analyses (**Fig. S5**). In addition, replacing K^+ with Cs^+, non-perovskite 4H and 3C perovskite phases are dominant microstructures at the final stage (240 s) in 5% Cs^+ film, while desired 3C perovskite phase dominates in 10% Cs^+ case. However, for 20% Cs^+ ink, halide-segregated perovskite phases dominate the microstructure.

Table 1 Summary of dominant phases comparison before and after TA for $FA_{0.85-x}MA_{0.15}K_xPbI_{2.55}Br_{0.45}$ and $FA_{0.85-y}MA_{0.15}Cs_yPbI_{2.55}Br_{0.45}$ (x and y = 0.05, 0.1, and 0.2 respectively) hybrid perovskite thin films.

Microstructure	Thermal Annealing (TA)	$FA_{0.85-x}MA_{0.15}\mathbf{K}_xPbI_{2.55}Br_{0.45}$			$FA_{0.85-y}MA_{0.15}\mathbf{Cs}_yPbI_{2.55}Br_{0.45}$		
		x = 0.05	x = 0.1	x = 0.2	y = 0.05	y = 0.1	y = 0.2
Phases present	Before	4H	4H	4H	4H, 3C	3C	3C (α_1 & α_2)
	After	4H, 3C (α_1 & α_2)	4H, 3C	4H, 3C	3C	3C	4H, 3C (α_1 & α_2)
Non-perovskite phase(s) formed?	Before	Yes	Yes	Yes	Yes	no	no
	After	Yes	Yes	Yes	no	no	no
Perovskite phase formed?	Before	No	no	no	no	Yes	Yes (segregation)
	After	Yes (segregation)	Yes	Yes	Yes	Yes	Yes (segregation)

Due to the substantial differences in phase transformation behavior during spin coating as a result of K^+- and Cs^+ addition, it is expected that these formulations will also impact the morphology of perovskite thin films destined for solar cell devices. Therefore, we turn our attention to studying the morphology of $FA_{0.85-x}MA_{0.15}K_xPbI_{2.55}Br_{0.45}$ and $FA_{0.85-y}MA_{0.15}Cs_yPbI_{2.55}Br_{0.45}$ (x and y = 0.05, 0.1, and 0.2) formulations via optical and scanning electron microscopy (SEM). **Fig. 3a** and **3c** show comparative optical images of these films before and after TA. K^+-incorporated films appear with an orange color before TA and convert to black after TA, consistent with the observed formation of the 3C phase (**Fig. 2c** and **2d**), while these films are known to retain a certain fraction of the 4H phase. Cs^+-incorporated films are considerably darker prior to annealing, showing evidence of conversion during antisolvent drip or direct formation of the desirable 3C phase (**Fig. 2 and 3c**).

The morphology of Cs^+-doped films is less sensitive to Cs^+ content and consists of compact films with excellent substrate coverage (**Fig. 3d)**. However, in K^+-doped films, we observe multiple pinholes, cracks, and occasional elongated crystals (white) with increasing K^+ content (10 and 20% K^+-doped films in **Fig. 3b**). The top-view SEM image of $FA_{0.85}MA_{0.15}PbI_{2.55}Br_{0.45}$ perovskite without K^+ and Cs^+ cations thin film is shown in **Fig. S10a** for comparison. The bright regions in the SEM image could potentially indicate the presence of unconverted wide bandgap

and more insulating 4H non-perovskite phase and may result in perovskite phase segregation, which was observed in time-resolved GIWAXS results.[6a, 9e, 13] Most notably, some other papers also reported these bright regions might be PbX_2 (X = Cl, Br, and I) and a moderate excess of PbI_2 crystals in the perovskite film might reduce recombination via defects and be beneficial to solar cell performance.[19] While all films exhibit the perovskite phase after annealing, these micrographs clearly show that the phase transformation pathway, and in particular through direct conversion to 3C phase thanks to Cs^+ addition, is most helpful to achieving compact films with uniform grain size, which is expected to help avoid shorts and performance losses in solar cell devices.

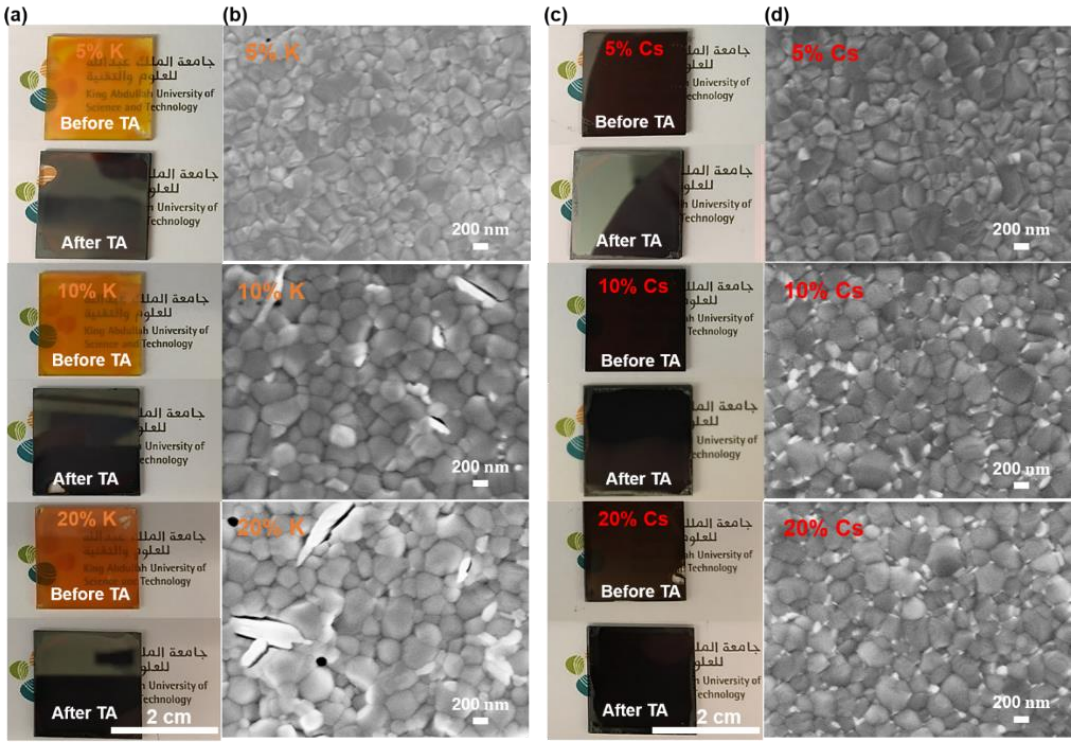

Figure 3. Comparison of various 3D hybrid K^+- and Cs^+-containing (5, 10, and 20 %) perovskite solid-state thin films. (a, c) Photographs of each perovskite thin film before and after thermal TA for 10 minutes at 100 °C. (b, d) Top-view SEM images of each 3D perovskite film prepared from various precursor inks.

We further evaluated the influences of K^+ and Cs^+ concentration on solid-state optical properties of mixed-cation and mixed-halide perovskite films. **Fig. 4a** shows the optical absorbance spectra of films with 5% to 20% K^+- and Cs^+-doped cations. The concentration of K^+

has little impact on the absorption spectrum (bandgaps ≈1.6 eV), while a higher concentration of Cs^+ blue-shifts the spectra and increases the optical bandgap from ≈1.6 eV to ≈1.66 eV (as shown Tauc plot in **Fig. S13)**. We have also investigated the impact of the layer's chemical composition on charge carrier transport via space-charge limited current (SCLC) measurements (**Fig. 4b**).[20] We collected dark current–voltage characteristics for electron-only devices based on various concentrations of K^+- and Cs^+-containing perovskite thin films. **Fig. S6** illustrates dark current–voltage characteristics of the representative $FA_{0.8}MA_{0.15}Cs_{0.05}PbI_{2.55}Br_{0.45}$ (5% Cs^+-doped film) perovskite device, indicating a linear ohmic response at the low bias (< 0.27 V), a trap-filling regime (0.28 V to 0.55 V) and a trap-free space-charge limited current (SCLC) regime (> 0.56 V). The trap state density was determined from the trap-filled limit voltage using the following equation:

$$N_t = \frac{2\varepsilon_0\varepsilon_r V_{TFL}}{qL^2} \quad (1)$$

where ε_0 is vacuum permittivity, ε_r is relative dielectric constant (ε_r = 46.9)[21], V_{TFL} onset voltage of trap-filled limit region, q elemental charge, and L thickness of film.[22] We found that N_t increases with increasing K^+ concentration from 5%, 10% to 20%, for $FA_{0.85-x}MA_{0.15}K_xPbI_{2.55}Br_{0.45}$ perovskite devices, yielding 2.60×10^{16}, 3.10×10^{16} and 4.44×10^{16} cm^{-3}, respectively (**Fig. S6a**). The replacement of K^+ by Cs^+ appears to reduce the concentration of traps where N_t is determined to be 2.05×10^{16}, 2.41×10^{16}, and 2.66×10^{16} cm^{-3} for 5%, 10%, and 20% Cs^+-containing perovskite layers, respectively (**Fig. S6b**). These results suggest that replacing K^+ with Cs^+ remediates defects, which is expected to diminish charge recombination, which in the case of solar cells may lead to increased fill factor (*FF*).

The intrinsic electron mobility was estimated using the SCLC method (**Fig. 4b**).[23] The electron mobility was further extracted using Mott–Gurney Law[24]:

$$\mu = \frac{8J_D L^3}{9\varepsilon_0\varepsilon_r V^2} \quad (2)$$

where J_D is current density and V is applied voltage. The electron mobility is found to be 1.54 cm^2 V^{-1} s^{-1} for the 5% K^+-incorporated film. The introduction of higher K^+ content decreases the electron mobility slightly to 1.12 and 1.13 cm^2 V^{-1} s^{-1} in the presence of 10% and 20% K^+ films, respectively. However, in the case of $FA_{0.75}MA_{0.15}Cs_{0.1}PbI_{2.55}Br_{0.45}$ device, the electron mobility increases to 2.11 cm^2 V^{-1} s^{-1}, which is higher than layers containing other Cs^+ concentrations, i.e., 5% and 20%. Although the addition of a small concentration of both K^+ and Cs^+ alkali cations

appears to enhance the carrier mobility, $FA_{0.75}MA_{0.15}Cs_{0.1}PbI_{2.55}Br_{0.45}$ exhibits the highest mobility partially due to the reduced trap states.[9e, 21, 25]

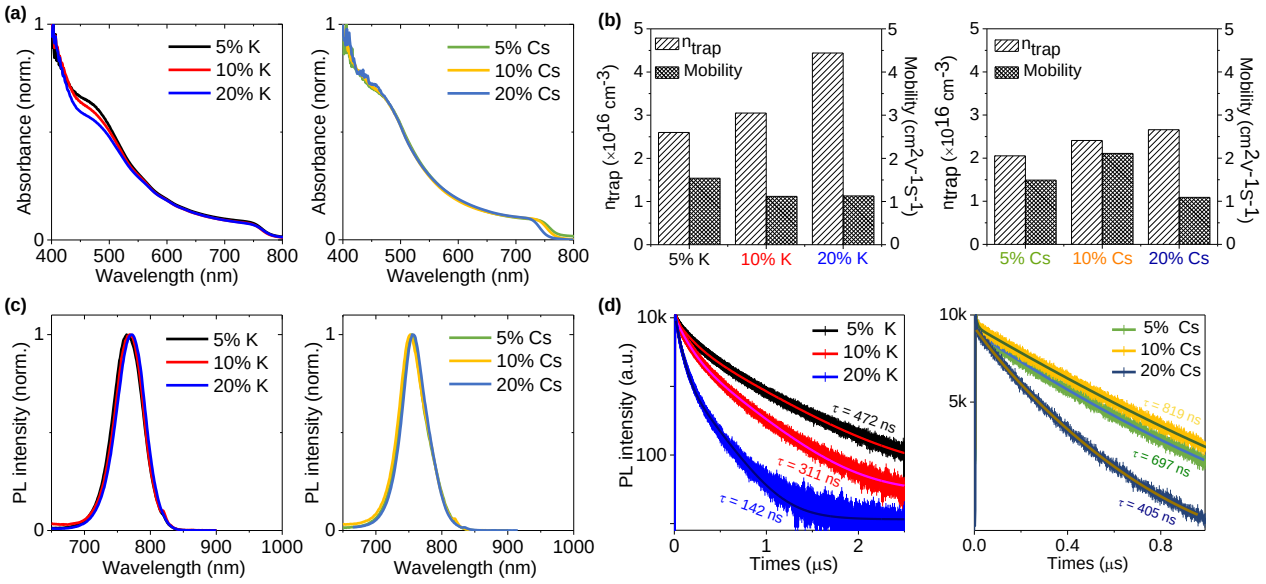

Figure 4. Comparison of various 3D hybrid K^+- and Cs^+-incorporated (5, 10, and 20 %) perovskite solid-state thin films. (a) Absorption (b) trap densities and electron mobilities (c) steady-state photoluminescence (PL) spectra and (d) time-resolved PL (TRPL) spectra for these perovskite thin films.

Fig. 4c presents steady-state photoluminescence (PL) spectra for these samples, showing the PL peak remaining at 768 (±4) nm for all films. The time-resolved PL (TRPL) analysis performed for the six perovskite films together with a summary of the fitting parameters used is shown in **Table S1**. The correlated parameters were fitted using a biexponential **Eq. 2** (**Fig. 4d**)[24a]

$$(t) = A_1 \exp(-t/\tau_1) + A_2 \exp(-t/\tau_2) + \mathrm{B} \qquad (3)$$

where τ_1 and τ_2 are slow and fast decay time constants, respectively, A_1 and A_2 are their corresponding amplitudes and B is a constant. The average carrier lifetimes evaluated are 472 ns, 311 ns, and 142 ns for 5%, 10%, and 20% K^+-doped perovskite films, respectively. While 5%, 10%, and 20% Cs^+-incorporated films have longer average carrier lifetimes evaluated are 697 ns, 819 ns, and 405 ns, respectively. We observe significantly longer lifetime for both 5% and 10% Cs^+-doped films. This observation implies that both 5 and 10% Cs^+-doped perovskite films should

exhibit smaller recombination losses, ultimately benefitting charge collection, *FF*, and open-circuit voltage (V_{OC}) of solar cells.[9e, 25]

Using the knowledge gained from the *in situ* and *ex situ* studies, we fabricated planar n-i-p type $FA_{0.85-x}MA_{0.15}K_xPbI_{2.55}Br_{0.45}$ and $FA_{0.85-y}MA_{0.15}Cs_yPbI_{2.55}Br_{0.45}$ (x and y = 0.05, 0.1, and 0.2 respectively) perovskite solar cells with the layer configuration (see inset in **Fig. 5b**): glass/ indium-doped tin oxide (ITO)/ compact titanium dioxide (c-TiO_2)/ perovskite layers/ 2,2′,7,7′-tetrakis-(*N*,*N*-di-pmethoxyphenylamine)-9,9′-spirobifluorene (Sprio-OMeTAD)/ gold (Au). All solar cells were characterized under standard AM1.5G (air mass 1.5 global 1 Sun) illumination with a scan rate of 0.1 V^{-1} s^{-1}. We first collected data on 20–25 solar cells based on $FA_{0.85-x}MA_{0.15}K_xPbI_{2.55}Br_{0.45}$ (**Fig. 5a and S7**), and compared them with $FA_{0.85}MA_{0.15}PbI_{2.55}Br_{0.45}$ (i.e. no K^+ and Cs^+) devices (**Fig. S10b**). Solar cells containing 5% K^+ exhibit an average PCE of 17.15 ± 0.62 %, with J_{SC} reaching approximately 22.95 ± 0.96 mA cm^{-2}, which is higher than devices containing higher K^+ concentrations and $FA_{0.85}MA_{0.15}PbI_{2.55}Br_{0.45}$ (i.e. no K^+ and Cs^+) devices (average PCE = 16.88 ± 0.84%). The lower PCE with increasing K^+ content is attributed to the deteriorated layer morphology (**Fig. 3**) and optoelectronic properties (**Fig. 4**). In **Fig. 5b**, we observed statistically meaningful improvements in device performance with replacement of K^+ by Cs^+ cation: PCE improves from 17.15 ± 0.62 % (5% K^+ device) to 19.24 ± 0.53 % (5% Cs^+ device). PCE further improves to 19.45 ± 0.40 % when further increasing Cs^+ to 10%. The average photovoltaic parameters of all the 3D $FA_{0.85-x}MA_{0.15}K_xPbI_{2.55}Br_{0.45}$ and $FA_{0.85-y}MA_{0.15}Cs_yPbI_{2.55}Br_{0.45}$ (x and y = 0.05, 0.1, and 0.2 respectively) hybrid perovskite solar cells are summarized in **Table S3** with all original *J-V* curves shown in **Fig. S11**. Higher PCE for the device with 10% Cs^+ is mainly attributed to enhancement in *FF* and J_{SC}, consistent with observations of improved film quality and optoelectronic properties (**Fig. 3 and 4**). This is not surprising considering that we see observable differences in film morphology and microstructure when using various perovskite precursor inks. These results suggest that tuning the composition of the perovskite inks can help to enhance the photovoltaic performance of the resulting devices.

We also observe PCE decrease for devices with high Cs^+ concentration. The 20% Cs+ concentration leads to PCE decrease to 14.63 ± 1.30 %. The PCE drop is in line with halide segregation (**Fig. 2 and 6**) and lower carrier mobility and carrier lifetime (**Fig. 4**). The deterioration of performance for devices with high K^+ and Cs^+ highlights the need to control phase formation

during film formation to eliminate non-perovskite phases and enhance PCE. We achieved a peak PCE of 20.75 % with V_{OC} = 1.18 V, J_{SC} = 23.68 mA cm^{-2} and FF = 72.93 % for the $FA_{0.75}MA_{0.15}Cs_{0.1}PbI_{2.55}Br_{0.45}$ perovskite solar cell (**Fig. 5c**) in reverse scan with little hysteresis (PCE = 20.03% in forward scan). The hysteretic behavior for all other perovskite solar cells with K^+ and Cs^+ cations addition are shown in **Fig. S12**. Key performance parameters extracted from the operating characteristics of the other perovskite devices are shown in **Fig. S7a-b**. In addition, external quantum efficiency (EQE) of the champion device (**Fig. 5d**), showing an integrated J_{SC} = 22.51 mA cm^{-2}, which is close to the measured J_{SC}.

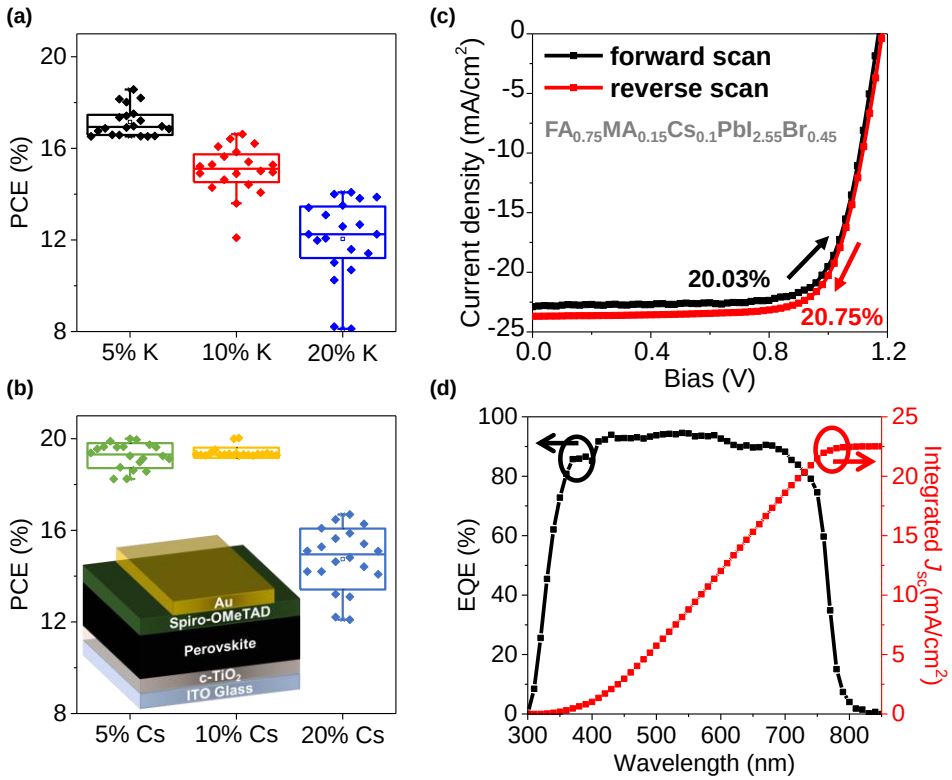

Figure 5. Solar cell architecture and characterization. (a) Statistics of 20-25 devices for each $FA_{0.85-x}MA_{0.15}K_xPbI_{2.55}Br_{0.45}$ and (b) $FA_{0.85-y}MA_{0.15}Cs_yPbI_{2.55}Br_{0.45}$ (x and y = 0.05, 0.1, and 0.2 respectively) perovskite solar cells. The inset figure shows a schematic diagram of representative perovskite solar cells used in this work. (c) *J–V* curve for the peak efficiency of 20.75% in the reverse scan (20.03% in the forward scan) obtained in the $FA_{0.75}MA_{0.15}Cs_{0.1}PbI_{2.55}Br_{0.45}$ perovskite solar cell under AM1.5G illumination. (d) External quantum efficiency (EQE) for the champion cell.

The environmental stability of the perovskite solar cells was also evaluated. Unencapsulated devices were exposed to an ambient environment with ≈50% relative humidity in the dark at room temperature. The normalized PCEs versus time were recorded periodically (**Fig. S7c)**. Devices incorporate small amounts of K^+ and Cs^+ (5% for K^+ and 5% and 10% for Cs^+) exhibit significantly improved environmental stability. For example, the PCEs retain 86%, 87%, 69%, 80%, 71% and 62% of its initial value for 5% Cs^+, 10% Cs^+, 20% Cs^+, 5% K^+, 10% K^+, and 20% K^+ doped solar cells after 50-day ambient exposure (50% RH conditions without encapsulation). The far superior ambient stability of 5% Cs^+, 10% Cs^+, and 5% K^+ doped devices is partially attributed to fewer phase impurities present in films[8] and to better phase stability since the addition of Cs^+ and K^+ helps to form an entropically stabilized phase.

To explain the observed differences in photovoltaic performance, we evaluated the electronic transport properties by using non-contact, time-resolved terahertz spectroscopy (TRTS)[26] for $FA_{0.85-y}MA_{0.15}Cs_yPbI_{2.55}Br_{0.45}$ (y = 0.05, 0.1, and 0.2 respectively) films (**Fig. 6**). TRTS is an ultrafast spectroscopic technique that utilizes a visible pump to generate carriers and a terahertz probe to interrogate the dynamics of free charge carrier pairs. **Fig. 6a** shows kinetic sweeps (varying pump-probe delay) of three Cs^+-doped perovskite samples, representing the relaxation kinetics of conduction by photogenerated charges. The strong temporal dependence of the photoconductive signal indicates that we must be judicious in selecting relative time delay for comparison. We selected 50 ps for measuring frequency-dependent conductivity to allow time for relaxation and emulate thermalized conduction at the cost of signal intensity. **Fig. 6b** shows complex, frequency-dependent photoconductivity data for each fit using the Drude-Smith model[27] for confined charge carriers. The flatter 10% and 20% Cs^+ responses suggest a more metallic-like character with constant charge scattering within confined domains. The zero frequency value of the real conductivity provides the most robust estimate of macroscopic conductivity and mobility fitted from the Drude-Smith model. **Table S2** summarizes the extracted conductivity and mobility data with confidence intervals. These values indicate each sample exhibits mobility of ≈ 1 cm^2/V s, in agreement with **Fig. 4b**, and that the 10% Cs^+-doped perovskite is ≈ 30 % more conductive than the other counterparts, which might partially explain the differences in photovoltaic performance. The thickness of each perovskite thin film was measured by ellipsometry (**Fig. S8**).

To further explore the effects of Cs^+ cation content, X-ray photoemission spectra (XPS) was utilized to investigate elemental composition (**Fig. S9)**, including C 1s, Pb 4f, I 3d, Br 3d, and Cs 3d (fitted by Lorentzian-Gaussian peaks) for 5% and 20% Cs^+-doped films. The Pb 4f for both films show a sharp doublet located at 137.9 eV (Pb $4f_{7/2}$) and 142.8 eV (Pb $4f_{5/2}$), which are assigned to Pb^{2+} metal ion. The peak positions of I $3d_{5/2}$ and Br $3d_{5/2}$ located at 618.8 eV and 68.0 eV are also consistent with the literature.[28] Both I $3d_{5/2}$ and Br $3d_{5/2}$ core level spectra include one single peak indicating these halides are present as only one chemical oxidation state in 5% and 20% Cs^+-doped films. The increased alkali metal cation concentrations can be observed through the higher intensity of Cs 3d peaks.

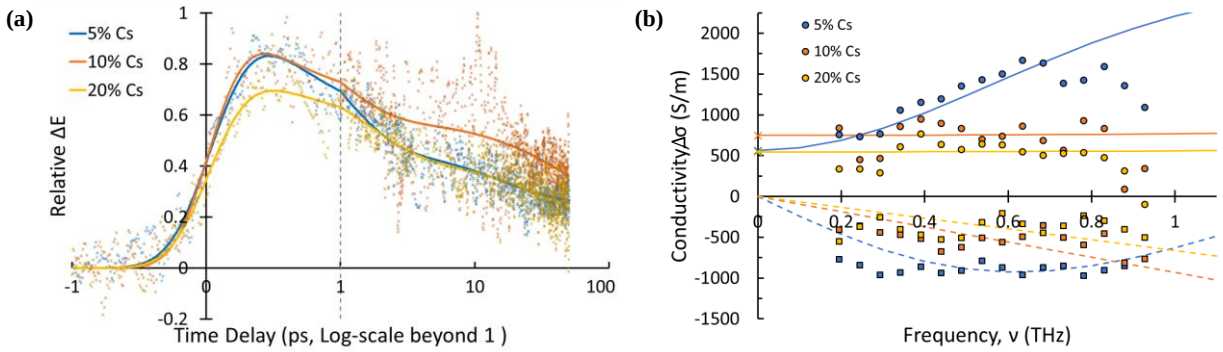

Figure 6. Terahertz mobility of spin-coated Cs^+-doped perovskite films determined by time-resolved terahertz spectroscopy (TRTS) at room temperature. (a) Time-dependence of ΔE for the Cs^+-doped perovskite films at pump-probe delay times out to 50 ps using 400 nm pump excitation. (b) Frequency-dependence of the real (circle/solid line) and imaginary (square/dashed line) parts of their photoconductivity at a 50 ps time delay and modeled with the Drude-Smith model.

Conclusion

In summary, we investigated several FA-dominated mixed-cation mixed-halide formulations with K^+ and Cs^+ doping impacts on microstructure transformation pathway via time-resolved GIWAXS measurements, associated with morphology, charge carrier mobility, trap state formation, and solar cell performance. K^+-doped formulations tend to form intermediate non-perovskite 4H phases from disordered solvate, rather than the desirable 3C perovskite-phase, during spin coating. TA treatment suppresses the 4H phase and promotes the formation of the 3C perovskite. In contrast, for Cs^+-doped formulations, 4H and 3C phases coexist and dominate the microstructure in 5% Cs^+-

containing films, while the desirable 3C phase dominates in layers with 10% Cs^+. Perovskite halide segregation dominates in layers with 20% Cs^+ content. SCLC and TRPL results confirm that a small amount of Cs^+ or K^+ introduction in films remediates trap states, enhances carrier mobility, and increases carrier lifetime. Both 5% and 10% Cs^+ perovskite solar cells yielded a peak PCE of over 20% with superior ambient stability. To our knowledge, the present work is one of the first to exploit *in situ* GIWAXS to shed light on the role of alkali metal cations mixing, as well as the role of antisolvent drip and TA on perovskite crystallization pathways. The essential new insights provide an in-depth understanding of perovskite ink drying and phase transformation dynamics, which is critically important for future ink design and the transfer of intricate perovskite processing recipes to manufacturing-relevant processes.

Author contributions

M.-C. T. and Y. F. contributed equally to this work. M.-C. T. designed and performed most of the *in situ* GIWAXS investigations. M.-C. T. and Y. F. conducted device fabrication and measurements of optoelectronic properties and SEM analysis. A. A., K. Z., and T. D. A. supervised the work. M.-C. T., D. B., R. L., and D.-M. S. assisted with *in situ* GIWAXS measurements. S. Z. and C. A. H. performed the XPS measurements. N. V. N. measured and simulated the ellipsometry spectra. T. M. and E. J. H. performed the time-resolved terahertz spectroscopy measurements. All authors provided critical feedback and helped the research, analysis, and manuscript.

Conflicts of interest

There are no conflicts to declare.

Acknowledgments

This work was supported by the King Abdullah University of Science and Technology (KAUST), and the National Key Research and Development Program of China (2017YFA0204800, 2016YFA0202403), National Natural Science Foundation of China (61604092, 61674098), National University Research Fund (Grant Nos. GK261001009, GK201603055), the 111 Project

(B14041), the National 1000 Talents Plan program (1110010341). GIWAXS measurements were performed at the D-line at the Cornell High Energy Synchrotron Source (CHESS) at Cornell University. CHESS is supported by the NSF and NIH/NIGMS via NSF Award DMR-1332208. Dr. Tang acknowledges support under the Cooperative Research Agreement between the University of Maryland and the National Institute of Standards and Technology Physical Measurement Laboratory, Award 70NANB14H209, through the University of Maryland. All the commercial instruments and materials mentioned here are identified to foster understanding. Such identification does not imply recommendation or endorsement by the National Institute of Standards and Technology, nor does it imply that the materials or equipment identified are necessarily the best available for the purpose.

References

[1] a) Q. Lin, A. Armin, R. C. R. Nagiri, P. L. Burn, P. Meredith, *Nat Photon* **2015**, 9, 106; b) A. Miyata, A. Mitioglu, P. Plochocka, O. Portugall, J. T.-W. Wang, S. D. Stranks, H. J. Snaith, R. J. Nicholas, *Nat Phys* **2015**, 11, 582; c) F. Hao, C. C. Stoumpos, R. P. Chang, M. G. Kanatzidis, *J. Am. Chem. Soc.* **2014**, 136, 8094; d) T. Liu, K. Chen, Q. Hu, R. Zhu, Q. Gong, *Adv Energy Mater* **2016**, 6, 1600457.

[2] V. Gonzalez-Pedro, E. J. Juarez-Perez, W. S. Arsyad, E. M. Barea, F. Fabregat-Santiago, I. Mora-Sero, J. Bisquert, *Nano Lett.* **2014**, 14, 888.

[3] N. R. E. Laboratory, Best Research-Cell Efficiencies Chart, https://www.nrel.gov/pv/assets/pdfs/best-research-cell-efficiencies-190416.pdf, accessed: 05 May, 2019.

[4] J. A. Christians, P. Schulz, J. S. Tinkham, T. H. Schloemer, S. P. Harvey, B. J. Tremolet de Villers, A. Sellinger, J. J. Berry, J. M. Luther, *Nat. Energy* **2018**, 3, 68.

[5] a) J. Sun, J. Wu, X. Tong, F. Lin, Y. Wang, Z. M. Wang, *Adv. Sci.* **2018**, 5, 1700780; b) J. M. Ball, A. Petrozza, *Nat. Energy* **2016**, 1, 1; c) Y. Hu, E. M. Hutter, P. Rieder, I. Grill, J. Hanisch, M. F. Aygüler, A. G. Hufnagel, M. Handloser, T. Bein, A. Hartschuh, K. Tvingstedt, V. Dyakonov, A. Baumann, T. J. Savenije, M. L. Petrus, P. Docampo, *Adv Energy Mater* **2018**, 8, 1703057.

[6] a) K. Wang, M. C. Tang, H. X. Dang, R. Munir, D. Barrit, M. De Bastiani, E. Aydin, D. M. Smilgies, S. De Wolf, A. Amassian, *Adv. Mater.* **2019**, 31, e1808357; b) M. Deepa, M. Salado, L. Calio, S. Kazim, S. M. Shivaprasad, S. Ahmad, *Phys. Chem. Chem. Phys.* **2017**, 19, 4069; c) D. J. Kubicki, D. Prochowicz, A. Hofstetter, S. M. Zakeeruddin, M. Gratzel, L. Emsley, *J. Am. Chem. Soc.* **2017**, 139, 14173; d) M. Abdi-Jalebi, Z. Andaji-Garmaroudi, S. Cacovich, C. Stavrakas, B. Philippe, J. M. Richter, M. Alsari, E. P. Booker, E. M. Hutter, A. J. Pearson, S. Lilliu, T. J. Savenije, H. Rensmo, G. Divitini, C. Ducati, R. H. Friend, S. D. Stranks, *Nature* **2018**, 555, 497; e) D. Y. Son, S. G. Kim, J. Y. Seo, S. H. Lee, H. Shin, D. Lee, N. G. Park, *J. Am. Chem. Soc.* **2018**, 140, 1358; f) J. Xu, C. C. Boyd, Z. J. Yu, A. F. Palmstrom, D. J. Witter, B. W. Larson, R. M. France, J. Werner, S. P. Harvey, E. J. Wolf, W. Weigand, S. Manzoor, M. F. A. M. van Hest, J. J. Berry, J. M. Luther, Z. C. Holman, M. D. McGehee, *Science* **2020**, 367, 1097.

[7] Z. Tang, T. Bessho, F. Awai, T. Kinoshita, M. M. Maitani, R. Jono, T. N. Murakami, H. Wang, T. Kubo, S. Uchida, H. Segawa, *Sci. Rep.* **2017**, 7, 12183.

[8] M. Saliba, T. Matsui, J. Y. Seo, K. Domanski, J. P. Correa-Baena, M. K. Nazeeruddin, S. M. Zakeeruddin, W. Tress, A. Abate, A. Hagfeldt, M. Gratzel, *Energy Environ. Sci.* **2016**, 9, 1989.

[9] a) Y. Zhang, P. Wang, M.-C. Tang, D. Barrit, W. Ke, J. Liu, T. Luo, Y. Liu, T. Niu, D.-M. Smilgies, Z. Yang, Z. Liu, S. Jin, M. G. Kanatzidis, A. Amassian, S. F. Liu, K. Zhao, *J. Am. Chem. Soc.* **2019**, 141, 2684; b) Y. Zhong, R. Munir, J. Li, M.-C. Tang, M. R. Niazi, D.-M. Smilgies, K. Zhao, A. Amassian, *ACS Energy Lett.* **2018**, 3, 1078; c) T. Niu, J. Lu, M.-C. Tang, D. Barrit, D.-M. Smilgies, Z. Yang, J. Li, Y. Fan, T. Luo, I. McCulloch, A. Amassian, S. Liu, K. Zhao, *Energy Environ. Sci.* **2018**, 11, 3358; d) Y. Zhong, R. Munir, A. H. Balawi, A. D. Sheikh, L. Yu, M.-C. Tang, H. Hu, F. Laquai, A. Amassian, *ACS Energy Lett.* **2016**, 1, 1049; e) M.-C. Tang, Y. Fan, D. Barrit, X. Chang, H. X. Dang, R. Li, K. Wang, D.-M. Smilgies, S. Liu, S. De Wolf, T. D. Anthopoulos, K. Zhao, A. Amassian, *J Mater Chem A* **2020**, 8, 1095; f) M. C. Tang, D. Barrit, R. Munir, R. P. Li, J. M. Barbe, D. M. Smilgies, S. Del Gobbo, T. D. Anthopoulos, A. Amassian, *Sol Rrl* **2019**, 3, 1800305; g) D. Barrit, P. Cheng, K. Darabi, M. C. Tang, D. M. Smilgies, S. Liu, T. D. Anthopoulos, K. Zhao, A. Amassian, *Adv. Funct. Mater.* **2020**, n/a, 1907442.

[10] a) K. Meng, L. Wu, Z. Liu, X. Wang, Q. Xu, Y. Hu, S. He, X. Li, T. Li, G. Chen, *Adv. Mater.* **2018**, 30, 1706401; b) T. Niu, J. Lu, X. Jia, Z. Xu, M. C. Tang, D. Barrit, N. Yuan, J. Ding, X. Zhang, Y. Fan, T. Luo, Y. Zhang, D. M. Smilgies, Z. Liu, A. Amassian, S. Jin, K. Zhao, S. F. Liu, *Nano Lett.* **2019**; c) S. Lee, M.-C. Tang, R. Munir, D. Barrit, Y.-J. Kim, R. Kang, J.-M. Yun, D.-M. Smilgies, A. Amassian, D.-Y. Kim, *J Mater Chem A* **2020**; d) M. Babics, R.-Z. Liang, K. Wang, F. Cruciani, Z. Kan, M. Wohlfahrt, M.-C. Tang, F. Laquai, P. M. Beaujuge, *Chem. Mater.* **2018**, 30, 789.

[11] Q. Hu, L. Zhao, J. Wu, K. Gao, D. Luo, Y. Jiang, Z. Zhang, C. Zhu, E. Schaible, A. Hexemer, C. Wang, Y. Liu, W. Zhang, M. Gratzel, F. Liu, T. P. Russell, R. Zhu, Q. Gong, *Nat. Commun.* **2017**, 8, 15688.

[12] D. Barrit, P. Cheng, M.-C. Tang, K. Wang, H. Dang, D.-M. Smilgies, S. Liu, T. D. Anthopoulos, K. Zhao, A. Amassian, *Adv. Funct. Mater.* **2019**, 29, 1807544.

[13] H. X. Dang, K. Wang, M. Ghasemi, M. C. Tang, M. De Bastiani, E. Aydin, E. Dauzon, D. Barrit, J. Peng, D. M. Smilgies, S. De Wolf, A. Amassian, *Joule* **2019**, 3, 1746.

[14] P. Gratia, I. Zimmermann, P. Schouwink, J. H. Yum, J. N. Audinot, K. Sivula, T. Wirtz, M. K. Nazeeruddin, *ACS Energy Lett.* **2017**, 2, 2686.

[15] J. Schlipf, P. Müller-Buschbaum, *Adv Energy Mater* **2017**, 7, 1700131.

[16] L. S. Ramsdell, *American Mineralogist* **1947**, 32, 64.

[17] a) A. Sharenko, C. Mackeen, L. Jewell, F. Bridges, M. F. Toney, *Chem Mater* **2017**, 29, 1315; b) L.-M. Wu, X.-T. Wu, L. Chen, *Coordination Chemistry Reviews* **2009**, 253, 2787.

[18] J. C. Hamill, J. Schwartz, Y.-L. Loo, *Acs Energy Lett* **2017**, 3, 92.

[19] a) T. J. Jacobsson, J.-P. Correa-Baena, E. Halvani Anaraki, B. Philippe, S. D. Stranks, M. E. F. Bouduban, W. Tress, K. Schenk, J. Teuscher, J.-E. Moser, H. Rensmo, A. Hagfeldt, *J. Am. Chem. Soc.* **2016**, 138, 10331; b) D. Bi, W. Tress, M. I. Dar, P. Gao, J. Luo, C. Renevier, K. Schenk, A. Abate, F. Giordano, J.-P. C. Baena, *Sci. Adv.* **2016**, 2, e1501170.

[20] T. Niu, J. Lu, R. Munir, J. Li, D. Barrit, X. Zhang, H. Hu, Z. Yang, A. Amassian, K. Zhao, S. F. Liu, *Adv. Mater.* **2018**, 30, e1706576.

[21] R. Singh, S. Sandhu, H. Yadav, J.-J. Lee, *ACS Appl. Mater. Interfaces* **2019**, 11, 29941.

[22] R. H. Bube, *J Appl Phys* **1962**, 33, 1733.

[23] Q. Han, S. H. Bae, P. Sun, Y. T. Hsieh, Y. M. Yang, Y. S. Rim, H. Zhao, Q. Chen, W. Shi, G. Li, Y. Yang, *Adv. Mater.* **2016**, 28, 2253.

[24] a) D. Barrit, P. Cheng, M.-C. Tang, K. Wang, H. Dang, D.-M. Smilgies, S. F. Liu, T. D. Anthopoulos, K. Zhao, A. Amassian, *Adv. Funct. Mater.* **2019**, 0, 1807544; b) Y. Fan, J. Fang, X. Chang, M.-C. Tang, D. Barrit, Z. Xu, Z. Jiang, J. Wen, H. Zhao, T. Niu, D.-M. Smilgies, S. Jin, Z. Liu, E. Q. Li, A. Amassian, S. Liu, K. Zhao, *Joule* **2019**, 3, 2485.

[25] H. Tan, F. Che, M. Wei, Y. Zhao, M. I. Saidaminov, P. Todorović, D. Broberg, G. Walters, F. Tan, T. Zhuang, B. Sun, Z. Liang, H. Yuan, E. Fron, J. Kim, Z. Yang, O. Voznyy, M. Asta, E. H. Sargent, *Nat. Commun.* **2018**, 9, 3100.

[26] a) R. Ulbricht, E. Hendry, J. Shan, T. F. Heinz, M. Bonn, *Rev Mod Phys* **2011**, 83, 543; b) D. Zhao, H. Hu, R. Haselsberger, R. A. Marcus, M. E. Michel-Beyerle, Y. M. Lam, J. X. Zhu, O. V. C. La, M. C. Beard, E. E. M. Chia, *ACS Nano* **2019**, 13, 8826.
[27] J. Lloyd-Hughes, T. I. Jeon, *J Infrared Milli Terahz Waves* **2012**, 33, 871.
[28] H. Xie, X. Liu, L. Lyu, D. Niu, Q. Wang, J. Huang, Y. Gao, *J. Phys. Chem. C* **2015**, 120, 215.